Numerical Modeling of Saline Gravity Currents Using EARSM and Buoyant k-ε Turbulence Closures

Mohammad Kazem Sharifian [1*], Kourosh Hejazi [2]

[1*] *Civil Eng. Department, K. N. Toosi University of Technology, Tehran, Iran; m.sharifian@sina.kntu.ac.ir.*
[2] *Civil Eng. Department, K. N. Toosi University of Technology, Tehran, Iran.*

ARTICLE INFO	ABSTRACT
	Gravity currents are very common in nature and may appear in rivers, lakes, oceans, and the atmosphere. They are produced by the buoyant forces interacting between fluids of different densities and may introduce sediments and pollutants into water bodies. In this study, the hydrodynamics and propagation of gravity currents are investigated using WISE (Width Integrated Stratified Environments), a 2DV hydrodynamic numerical model. An Explicit Algebraic Reynolds Stress Model (EARSM) has been deployed and implemented in the hydrodynamic model and the simulated results have been compared against the laboratory measured values and the results obtained from the k-ε buoyant turbulence model originally implemented in WISE. The numerical simulations focus on three types of gravity currents generated for laboratory experiments, namely: Lock-exchange gravity current, buoyant wall-jet flow and intrusive gravity current. The simulated evolution profiles and propagation velocities are compared with measured values. The numerical model shows good quantitative agreements for predicting the temporal and spatial evolution of the gravity currents. The simulation results show better agreements in case of EARSM compared to buoyant k-ε turbulence closure. A sensitivity study also has been conducted to investigate the influence of the values of spatial and temporal increments on the accuracy of the prediction for the turbulence closures.

1. Introduction

Gravity currents are flows driven by difference in density between the current itself and its surroundings. The difference in density may be caused by variations in mixture composition or temperature. The occurrence of density-driven gravity flows is widespread in nature. Sea breezes, snow avalanches, and thunderstorm microbursts are examples of density currents occurring in the atmosphere, while turbidity currents and saline density currents are examples that occur in the aquatic environment. The monograph of Simpson [1] contains many examples of natural and man-made gravity currents. Laboratory gravity currents may also be categorized as intrusion type or lock-exchange type. In the intrusion-type flows, the dense fluid enters the domain through an inlet underneath the ambient fluid, while in the lock-exchange type two fluids are separated initially by a gate. As the gate is removed in the lock-exchange configuration, the fluids suddenly become in contact and the heavier fluid spreads horizontally underneath

the lighter fluid. Several laboratory experiments have been performed to study gravity currents [2-6].

Numerical models are important tools which may be employed to investigate the evolution and impact of density currents. These models are not limited by the scale restrictions of experimental studies but may have limitation due to numerical solution. A number of Direct Numerical Simulations (DNS) and Large Eddy Simulations (LES) of gravity currents have been reported in the literature [7-11]. DNS and LES are powerful turbulence simulation tools but due to the strong dependence of the required spatial and temporal resolution to the Reynolds number, are inherently restricted to low Reynolds numbers and are not feasible for field-scale simulations. Reynolds-Averaged Navier-Stokes (RANS) models are usually preferred for such investigations, as they are computationally less demanding than DNS or LES. Among various RANS approaches, the eddy viscosity models (EVM) like two-equation k-ε models, have received the most attention due to their simple form and affordable computational cost [12-15]. Such

models, however, lack the correct description of some important physical aspects, and may give poor results in more complex flow situations, e.g. in the presence of buoyancy effects [16]. Differential Reynolds-stress models (DRSM) incorporate more physics than the standard two-equation models and are more widely applicable, but these models require solving additional transport equations for the different stress components, which could result in numerical difficulties. Good alternatives to DRSMs are Algebraic Reynolds Stress Models (ARSMs) that are derived directly from the transport equations for the Reynolds stresses and the turbulent flux. Such models may be obtained by applying the weak-equilibrium assumption, first formulated by Rodi [17], which states that both the advection and diffusion terms of normalized stresses and fluxes may be neglected. This leads to algebraic equations for the different components of the Reynolds stresses and the scalar flux. Instabilities are a major problem of early ARSM models due to their implicit solution method [16]. Therefore, there has been a considerable renewed interest in developing explicit models, which are the so-called Explicit Algebraic Reynolds Stress Models (EARSM). Recent advances for this class of models are those of Gatski and Speziale [18], Girimaji [19], Jongen and Gatski [20] and Wallin and Johansson [21]. To a large extent, these models have the same advantages as DRSM while require less computational effort [16]. The objective of the present study is to explore the dynamics of gravity currents using WISE, a 2DV hydrodynamic numerical model [22], by two different turbulence closures, the standard *k-ε* model with buoyancy terms and an Explicit Algebraic Reynolds Stress Model (EARSM) developed herein. The ability of the numerical model to predict the behavior of various important hydrodynamic features of gravity currents, such as propagation profiles and velocity distribution is confirmed by comparing the numerical simulations with the laboratory measured values reported in literature. Lock-exchange, wall jet flow and intrusive gravity currents have been simulated and the numerical predictions employing buoyant *k-ε* and EARSM turbulence closures have been compared against measured values.

2. Mathematical Modelling
2.1. Governing Equations
The governing equations deployed to describe the hydrodynamics of saline gravity currents are 2D width integrated continuity, momentum and scalar transport equations:

$$\frac{\partial u}{\partial x} + \frac{\partial w}{\partial z} = 0 \tag{1}$$

$$\frac{\partial u}{\partial t} + \frac{\partial u^2}{\partial x} + \frac{\partial wu}{\partial z} - w_g \frac{\partial u}{\partial z}$$
$$= -\frac{1}{\rho_r}\frac{\partial p}{\partial x} + \frac{\partial}{\partial x}\left(\nu \frac{\partial u}{\partial x}\right) + \frac{\partial}{\partial z}\left(\nu \frac{\partial u}{\partial z}\right) \tag{2}$$
$$- \frac{\partial}{\partial x}\left(\overline{u'u'}\right) - \frac{\partial}{\partial z}\left(\overline{u'w'}\right)$$

$$\frac{\partial w}{\partial t} + \frac{\partial wu}{\partial x} + \frac{\partial w^2}{\partial z} - w_g \frac{\partial w}{\partial z}$$
$$= -\frac{1}{\rho_r}\frac{\partial p}{\partial z} + \frac{\partial}{\partial x}\left(\nu \frac{\partial w}{\partial x}\right) + \frac{\partial}{\partial z}\left(\nu \frac{\partial w}{\partial z}\right) \tag{3}$$
$$- \frac{\partial}{\partial x}\left(\overline{u'w'}\right) - \frac{\partial}{\partial z}\left(\overline{w'w'}\right) - g\frac{\rho - \rho_r}{\rho_r}$$

$$\frac{\partial c}{\partial t} + \frac{\partial uc}{\partial x} + \frac{\partial wc}{\partial z} - w_g \frac{\partial c}{\partial z}$$
$$= \frac{\partial}{\partial x}\left(\frac{\nu}{\sigma_t}\frac{\partial c}{\partial x}\right) + \frac{\partial}{\partial z}\left(\frac{\nu}{\sigma_t}\frac{\partial c}{\partial z}\right) \tag{4}$$
$$- \frac{\partial}{\partial x}\left(\overline{u'c'}\right) - \frac{\partial}{\partial z}\left(\overline{w'c'}\right)$$

where *x* and *z* are the horizontal and vertical directions in Cartesian coordinate system respectively, *u* and *w* the horizontal and vertical mean velocity components respectively, *c* the salinity, *p* the pressure, ρ_r and ρ the reference density and density of the fluid respectively, ν the kinematic viscosity, *g* the gravitational acceleration and w_g the grid velocity. σ_t is the turbulent Schmit number and the prime symbol shows the fluctuating quantities. Terms $\overline{u'_i u'_j}$ and $\overline{u'_i c'}$ are Reynolds stress and Reynolds flux tensors respectively.

2.2. Turbulence Modelling
In this study two different closures of turbulence models; the standard *k-ε* model with buoyancy terms and an Explicit Algebraic Reynolds Stress model (EARSM) with an Explicit Algebraic Scalar Flux (EASFM) model for Reynolds fluxes, have been implemented.

The standard buoyancy-modified *k-ε* model [23] is based on the eddy-viscosity/diffusivity concept of Boussinesq, which uses an isotropic eddy-viscosity/diffusivity to relate the Reynolds stresses $\overline{u'_i u'_j}$ and turbulent fluxes $\overline{u'_i c'}$ of concentration to the mean field [23]:

$$-\overline{u'_i u'_j} = \nu_t \left(\frac{\partial u_i}{\partial x_j} + \frac{\partial u_j}{\partial x_i}\right) - \frac{2}{3}k\delta_{ij} \tag{5}$$

$$-\overline{u'_i c'} = -\Gamma \frac{\partial c}{\partial x_i} = -\frac{\nu_t}{\sigma_t}\frac{\partial c}{\partial x_i} \tag{6}$$

In equations (5) and (6) u_i and u'_i are the mean and fluctuating velocity components in x_i direction respectively, *c* and c' are the mean and fluctuating concentration, ν_t is the turbulent or eddy viscosity, Γ

is turbulent diffusivity of concentration, and σ_t is the turbulent Schmidt number which relates eddy viscosity to the eddy diffusivity and its value is an indication of the level of turbulent mixing. The production and dissipation of turbulent kinetic energy are subject to transport process. Thus, to describe the evolution of turbulence, two transport equations for turbulent kinetic energy, k, and the dissipation rate of energy, ε, in tensorial form are as follows [23]:

$$\frac{\partial k}{\partial t} + u_i \frac{\partial k}{\partial x_i} = \frac{\partial}{\partial x_i}\left(\frac{\nu_t}{\sigma_k}\frac{\partial k}{\partial x_i}\right) + P + G - \varepsilon \qquad (7)$$

$$\begin{aligned}\frac{\partial \varepsilon}{\partial t} + u_i \frac{\partial \varepsilon}{\partial x_i} &= \frac{\partial}{\partial x_i}\left(\frac{\nu_t}{\sigma_\varepsilon}\frac{\partial \varepsilon}{\partial x_i}\right) \\ &+ c_{1\varepsilon}\frac{\varepsilon}{k}(P + G)\left(1 + c_{3\varepsilon}R_f\right) - c_{2\varepsilon}\frac{\varepsilon^2}{k}\end{aligned} \qquad (8)$$

where P represents the production of k by interaction of Reynolds stresses and mean velocity gradient, and G represents the production/destruction of turbulence by buoyancy [23] as described by equations (9) and (10).

$$\begin{aligned}P &= -\overline{u'_i u'_j}\left(\frac{\partial u_i}{\partial x_j}\right) \\ &= \nu_t\left(\frac{\partial u_i}{\partial x_j} + \frac{\partial u_j}{\partial x_i}\right)\frac{\partial u_i}{\partial x_j}\end{aligned} \qquad (9)$$

$$G = -\beta g_i \overline{u'_i c'}\frac{\partial u_i}{\partial x_j} = \beta g_i \frac{\nu_t}{\sigma_t}\frac{\partial c}{\partial x_i} \qquad (10)$$

In the k-ε model the eddy viscosity, ν_t, relates to k and ε via Eq. (11), which is obtained from dimensional analysis and eddy viscosity concept [24]:

$$\nu_t = c_\mu \frac{k^2}{\varepsilon} \qquad (11)$$

In above equations $c_{1\varepsilon}$, $c_{2\varepsilon}$, $c_{3\varepsilon}$, β, and c_μ are empirical constants, g_i is the acceleration in x_i direction, and R_f is the flux Richardson number. Empirical constants of standard k-ε model are tabulated in Table 1 [23].

Table 1. Parameters of standard k-ε model

c_μ	σ_k	σ_ε	$c_{1\varepsilon}$	$c_{2\varepsilon}$	σ_t
0.09	1.0	1.3	1.4	1.92	1.0

The Explicit Algebraic Reynolds Stress Model (EARSM) has played a significant role in environmental hydraulics [25-26], especially in simulating anisotropic problems of stratified flows with different densities. Considering the buoyancy, streamline curvature and rotation effect, etc., the advantages of these models are particularly obvious compared with the two-equation turbulent models. In

this study the EARSM turbulence closure proposed by Wallin and Johansson [21] has been deployed. Algebraic Reynolds Stress Models belong to the family of nonlinear models. However, they are derived from the full Reynolds stress transport equation. The equation may be presented as [21]:

$$\begin{aligned}&\frac{k}{\varepsilon}\frac{Da_{ij}}{Dt} - \frac{1}{\varepsilon}\left(\frac{\partial T_{ijl}}{\partial x_l} - \frac{\overline{u'_i u'_j}}{k}\frac{\partial T_l^{(k)}}{\partial x_l}\right) \\ &= \frac{\overline{u'_i u'_j}}{k}\left(\frac{P}{\varepsilon} - 1\right) + \frac{P_{ij}}{\varepsilon} - \frac{\varepsilon_{ij}}{\varepsilon} + \frac{\phi_{ij}}{\varepsilon}\end{aligned} \qquad (12)$$

where a_{ij} is the anisotropy tensor of Reynolds stresses, and $-T_{ijl}$ and $-T_l^{(k)}$ are the turbulent and molecular fluxes of the Reynolds stress and turbulent kinetic energy, respectively. The dissipation rate tensor, ε_{ij}, and the pressure-strain rate tensor, ϕ_{ij}, need to be modelled whereas the production terms, $P_{ij} = -\overline{u'_i u'_j}\left(\partial u_i / \partial x_j\right)$ and $P = P_{ij}/2$, do not need any modelling since they are explicit in the Reynolds stress tensor.

Many inhomogeneous flows of engineering interest are steady flows and satisfy the weak equilibrium assumption [17]. In this case it is possible to neglect the advection and diffusion terms. The advection term is indeed exactly zero for all stationary parallel mean flows, such as fully developed channel and pipe flows [21]. For inhomogeneous flows the assumption of negligible effects of diffusion in the anisotropy tensor can cause some problems, particularly in regions where the production term is small or where the inhomogeneity is strong. However, this assumption has been found to be a reasonable approximation of the full differential Reynolds stress transport equations in a number of flow situations, and in many respects is superior to the eddy-viscosity hypothesis [21]. In the EARSM turbulence closure of Wallin and Johansson, invoking weak equilibrium condition results in [21]:

$$\frac{\overline{u'_i u'_j}}{k}\left(\frac{P}{\varepsilon} - 1\right) = \frac{P_{ij}}{\varepsilon} - \frac{\varepsilon_{ij}}{\varepsilon} + \frac{\phi_{ij}}{\varepsilon} \qquad (13)$$

By using appropriate models for the dissipation rate tensor ε_{ij} and the pressure-strain rate tensor ϕ_{ij} [21] and substituting, the following implicit form may be then obtained:

$$\begin{aligned}&\left(C_1 - 1 + \frac{P}{\varepsilon}\right)a_{ij} = -\frac{15}{8}S_{ij}^\tau \\ &+ \frac{4}{9}\left(a_{ik}W_{kj}^\tau - W_{ik}^\tau a_{kj}\right)\end{aligned} \qquad (14)$$

where $S_{ij}^\tau = S_{ij}\frac{k}{\varepsilon}$ and $W_{ij}^\tau = W_{ij}\frac{k}{\varepsilon}$ are written in terms of rate of strain and vorticity tensors:

$$S_{ij} = \frac{1}{2}\left(\frac{\partial u_i}{\partial x_j} + \frac{\partial u_j}{\partial x_i}\right),$$
$$W_{ij} = \frac{1}{2}\left(\frac{\partial u_i}{\partial x_j} - \frac{\partial u_j}{\partial x_i}\right) \qquad (15)$$

Eq. (14) may be rewritten in a matrix notation:

$$N\mathbf{a} = -\frac{6}{5}\mathbf{S}^\tau + (\mathbf{a}\mathbf{W}^\tau - \mathbf{W}^\tau \mathbf{a}) \qquad (16)$$

where N is related to the production-dissipation ratio by $N = \frac{9}{4}\left(C_1 + 1 + \frac{P}{\varepsilon}\right)$. Following the procedure proposed by Pope [27], Wallin and Johansson [21] proposed a general relation for the Reynolds stress anisotropy tensor, $\mathbf{a}$, by using a ten-tensor equation in terms of $\mathbf{S}^\tau$ and $\mathbf{W}^\tau$ for three-dimensional flows:

$$\mathbf{a} = \beta_1 \mathbf{S}^\tau + \beta_2 \left(\mathbf{S}^{\tau 2} - \frac{1}{3}II_S \mathbf{I}\right)$$
$$+\beta_3 \left(\mathbf{W}^{\tau 2} - \frac{1}{3}II_W \mathbf{I}\right) + \beta_4(\mathbf{S}^\tau \mathbf{W}^\tau - \mathbf{W}^\tau \mathbf{S}^\tau)$$
$$+\beta_5(\mathbf{S}^{\tau 2}\mathbf{W}^\tau - \mathbf{W}^\tau \mathbf{S}^{\tau 2})$$
$$+\beta_6 \left(\mathbf{S}^\tau \mathbf{W}^{\tau 2} - \mathbf{W}^{\tau 2}\mathbf{S}^\tau - \frac{2}{3}IV\mathbf{I}\right) \qquad (17)$$
$$+\beta_7 \left(\mathbf{S}^{\tau 2}\mathbf{W}^\tau - \mathbf{W}^\tau \mathbf{S}^{\tau 2} - \frac{2}{3}V\mathbf{I}\right)$$
$$+\beta_8(\mathbf{S}^\tau \mathbf{W}^\tau \mathbf{S}^{\tau 2} - \mathbf{S}^{\tau 2}\mathbf{W}^\tau \mathbf{S}^\tau)$$
$$+\beta_9(\mathbf{W}^\tau \mathbf{S}^\tau \mathbf{W}^{\tau 2} - \mathbf{W}^{\tau 2}\mathbf{S}^\tau \mathbf{W}^\tau)$$
$$+\beta_{10}(\mathbf{W}^\tau \mathbf{S}^{\tau 2}\mathbf{W}^{\tau 2} - \mathbf{W}^{\tau 2}\mathbf{S}^{\tau 2}\mathbf{W}^\tau)$$

where the β_i coeffcients may be functions of the five independent invariants in terms of $\mathbf{S}^\tau$ and $\mathbf{W}^\tau$ ($II_S = \{\mathbf{S}^{\tau 2}\}$, $II_W = \{\mathbf{W}^{\tau 2}\}$, $III_S = \{\mathbf{S}^{\tau 3}\}$, $IV = \{\mathbf{S}^\tau \mathbf{W}^{\tau 2}\}$, $V = \{\mathbf{S}^{\tau 2}\mathbf{W}^{\tau 2}\}$). By inserting Eq. (17) into Eq. (16) and using the Cayley-Hamilton theorem to reduce the higher-order tensor groups, β_i coefficients are obtained. For two-dimensional flows, there are three independent groups: $\mathbf{S}^\tau$, $\left(\mathbf{S}^{\tau 2} - \frac{1}{3}II_S \mathbf{I}\right)$ and $(\mathbf{S}^\tau \mathbf{W}^\tau - \mathbf{W}^\tau \mathbf{S}^\tau)$ and only β_1 and β_4 are non-zero coefficients. Then, the representation for $\mathbf{a}$ is formed as [21]:

$$\mathbf{a} = \beta_1 \mathbf{S}^\tau + \beta_4(\mathbf{S}^\tau \mathbf{W}^\tau - \mathbf{W}^\tau \mathbf{S}^\tau) \qquad (18)$$

where $\beta_1 = -\frac{6}{5}\frac{N}{N^2 - 2II_W}$; $\beta_4 = -\frac{6}{5}\frac{1}{N^2 - 2II_W}(\mathbf{S}^\tau \mathbf{W}^\tau - \mathbf{W}^\tau \mathbf{S}^\tau)$.

Now, from Eq. (18), a cubic equation for the unknown N may be obtained:

$$N^3 - C_1'N^2 - \left(\frac{27}{10}II_S + 2II_W\right)N + 2C_1'II_W \qquad (19)$$
$$= 0$$

where $C_1' = \frac{9}{4}(C_1 - 1)$. The above equation may be solved in a closed form with the solution for the positive root being:
for $P_2 \geq 0$:

$$N = \frac{C_1'}{3} + \left(P_1 + \sqrt{P_2}\right)^{1/3}$$
$$+\text{sign}\left(P_1 + \sqrt{P_2}\right)\left|P_1 + \sqrt{P_2}\right|^{1/3} \qquad (20)$$

and for $P_2 < 0$:

$$N = \frac{C_1'}{3} + (P_1^2 + P_2)^{1/6}$$
$$\times \cos\left(\frac{1}{3}\cos^{-1}\left[\frac{P_1}{\sqrt{P_1^2 - P_2}}\right]\right) \qquad (21)$$

where the P_1 and P_2 are defined as:

$$P_1 = \left(\frac{C_1'^2}{27} + \frac{9}{20}II_S - \frac{2}{3}II_W\right)C_1'$$
$$P_2 = P_1^2 - \left(\frac{C_1'^2}{9} + \frac{9}{10}II_S + \frac{2}{3}II_W\right)^3 \qquad (22)$$

In the model of Wallin and Johansson, the buoyancy effect was not considered. For anisotropic buoyant turbulent flows like saline gravity currents, the buoyancy effect should not be neglected in general, so, linear hypothesis was assumed in this study and Reynolds stresses are considered as the sum of $\overline{u'_i u'_j}|_s$ by strain and $\overline{u'_i u'_j}|_b$ by buoyancy:

$$\overline{u'_i u'_j} = \overline{u'_i u'_j}|_s + \overline{u'_i u'_j}|_b \qquad (23)$$

where $\overline{u'_i u'_j}|_s$ is the same as that in the EARSM proposed by Wallin and Johansson [21]. The algebraic expression proposed by Rodi [28] was adopted to express the last term in Eq. (23):

$$\overline{u'_i u'_j}|_b = \frac{(1 - c_3)\frac{k}{\varepsilon}G\left(\frac{G_{ij}}{G} - \frac{2}{3}\delta_{ij}\right)}{(c_1 + \frac{P+G}{\varepsilon} - 1)} \qquad (24)$$

where $G_{ij} = -\beta g_i \overline{u'_j c} - \beta g_i \overline{u'_i c}$; $G = -\beta g_i \overline{u'_j c}$; k is the turbulent kinetic energy; ε is the turbulent dissipation rate. $\overline{u'_i u'_j}$ in P is simplified as $\overline{u'_i u'_j}|_s$ here, and c_I=0.22 and c_3=0.55 are the constant parameters [28].

In order to model the Reynolds scalar flux accurately, the Explicit Algebraic Scalar Flux model of Hua et al. [29] has been deployed. This model is based on EASFM of Wikström et al. [30] and includes the buoyancy effects in the algebraic relation. The model may be written as:

$$\overline{u'_i c'}$$
$$= -(1 - c_{\theta 4})A_{ij}^{-1}\frac{k}{\varepsilon}\overline{u'_j u'_k}\frac{\partial c}{\partial x_k}$$
$$-(\frac{c_{\theta 6} - 1}{c_\theta})A_{ij}^{-1}\frac{k^2}{\varepsilon^2}\beta g_j \overline{u'_k c'}\frac{\partial c}{\partial x_k} \qquad (25)$$

46

Details may be found in [29].

2.3. Numerical Method

WISE (Width Integrated Stratified Environments) is an Arbitrary Lagrangian-Eulerian (ALE) 2D vertical hydrodynamic numerical model [22], based on time dependent Reynolds-Averaged Navier-Stokes (RANS) equations. The model is further refined and developed herein for EARSM turbulence closure. A structured non-orthogonal curvilinear staggered mesh is used for computational domain. Finite volume method has been utilized to discretize flow and momentum equations as well as transport equations of scalar quantities like salinity, concentration, k, ε, and also Reynolds stresses and fluxes. Finite volume method provides flexibility for defining control volumes in a staggered grid system, especially near bed and water surface, where rapid changes of bathymetry and free surface may have significant effect on the prediction of the flow flied. Moreover, the finite volume method, if accurately implemented, provides the assurance of global conservation.

In the ALE method the mesh motion may be chosen arbitrarily; the newly updated free surface is determined purely by Lagrangian method, by the velocity of fluid particles at the free surface, while in horizontal direction the grids are fixed. The grid geometry is computed and redistributed after completion of each time step. With this consideration, an additional grid velocity w_g, appears in the the Navier-Stokes and scalar transport equations.

The projection (fractional-step) method, proposed by Chorin [31] and Temam [32], has been adopted. The method generally is accomplished in two steps [22]; the pressure gradient terms are omitted from the momentum equations in the first step and the transport part of Navier-Stokes equations including advection and diffusion are advanced in time to obtain a provisional velocity field U^*. In the second step, the provisional velocity is corrected by accounting for the pressure gradient and continuity constraint as follows:

$$\frac{U^{n+1} - U^*}{\Delta t} + \nabla P^{n+1} = 0 \tag{26}$$

subject to the continuity constraint:

$$div U^{n+1} = 0 \tag{27}$$

By taking the divergence of (26), the continuity equation will be exerted and the Poisson equation is obtained:

$$\nabla^2 P^{n+1} = \frac{div U^*}{\Delta t} \tag{28}$$

From the above equations the pressure distribution is obtained and the velocity quantities are then updated. Advection and diffusion parts of transport equations

were computed in a locally one-dimensional manner in sub-fractional-steps in two directions. A fifth degree accurate scheme for advection and the Crank-Nicolson method for diffusion computations were utilized [22].

2.4. Boundary Conditions
2.4.1. Spatial Boundary Conditions

Spatial boundary conditions have been determined for free surface, rigid surfaces including bed and walls, and inlet and outlet boundaries for flow, transport of species and turbulence parameters. The kinematic boundary condition at the impermeable bottom gives:

$$u \frac{\partial z_b}{\partial x} + w = 0 \tag{29}$$

where z_b is the bed elevation above datum. Similarly, the kinematic boundary condition at the moving free surface is:

$$\frac{\partial \eta}{\partial t} + u \frac{\partial \eta}{\partial t} = w \tag{30}$$

where $\eta(x, t)$ is the free surface elevation. To keep the consistency, the free surface equation is obtained by integrating the continuity equation over depth and by the application of the kinematic conditions at bed (Eq. 29) and free surface (Eq. 30) as follows:

$$\frac{\partial \eta}{\partial t} + \frac{\partial}{\partial x} \int_{z_b}^{\eta} u dz = 0 \tag{30}$$

At inlet and outlet boundaries the velocity, pressure or water elevation may be regarded as known values depending on circumstances. In the case of the known velocity or pressure values, the corresponding distribution is applied at the boundary. For the outlet boundary a constant pressure was imposed. It was further assumed that the flow was fully developed at the outlet and the vertical derivative of the velocity components was set to zero [22]. At wall boundaries zero normal velocity and no-slip boundary conditions were considered. On the free surface, Neumann boundary for k and Dirichlet boundary for ε were used and set to zero. Neumann boundary values for k and ε were set to zero at the outlet. At the inlet boundary, it is assumed that the flow is smooth, and k and ε are set to small values different from zero.

2.4.2 Temporal Boundary Conditions

The initial velocity and pressure values are set equal to zero. k and ε are set to suitable values to give an appropriate kinematic value for viscosity.
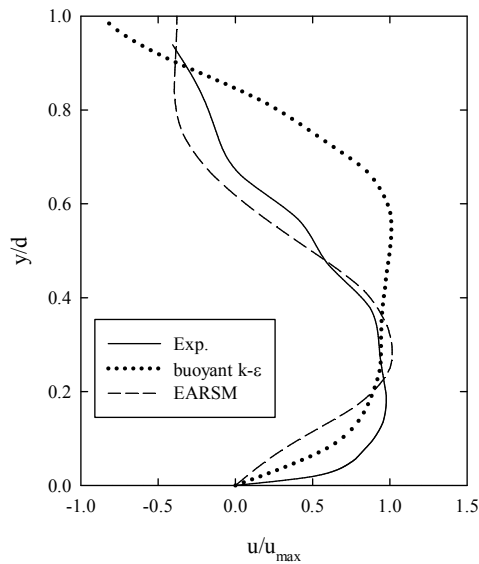
Figure 1. Velocity profiles of turbulence models and measured values in experiment of Kneller et al. [33]

3. Results and Discussion

In order to validate the new EARSM turbulence model and to investigate the predicted results and compare them with the simulated values obtained from k-ε turbulence closure, the predicted values for hydrodynamic parameters have been compared with the measured values of four experimental studies of lock-exchange and intrusive type and wall jet flows. These types of flows may represent gravity currents in estuaries.

The first test is based on the experimental data reported by Kneller et al. [33]. The experimental apparatus consisted of a simple rectangular lock-exchange tank, 0.2m wide and 2.15m long, and a 0.34m long lock compartment at one end. The flume was filled with ambient fluid to a depth of 0.1m. The lock compartment was filled to equal depth, and the density difference between saline and fresh water was 41 kg/m³. For simulation, 20 layers with 100 grids of dimension 0.025m in x-direction have been used to construct the domain. The simulation time was 40s and a time step of 0.05s has been used. Figure 1 shows the velocity profile comparison of two models with measured values at x=800mm and t=14s. y is the depth of the flow from bottom and d is the total depth of the flow. Velocities have been normalized for the maximum velocity. Better agreement has been obtained for EARSM; however at the boundaries buoyant k-ε closure, shows closer results.

The second test is a buoyant wall-jet flow, studied experimentally by Gerber [34]. The experiment was carried out in a Perspex flume with an inlet for the salt current with an excess density of 2 kg/m³ with respect to water, and discharge of 0.59 l/s. The gravity current was planned to travel along the flume bottom and exit it to a damping tank to prevent creation of a reverse flow to the upstream. The general characteristics of flow and inlet conditions utilized in laboratory

experiment by Gerber [34] and in the simulations are summarized in Table 2.

Table 2. Summary of general characteristics and inlet flow conditions in experiment of Gerber [34]

Parameter	Units	Value
water depth in flume	m	0.30
depth of inlet current	m	0.03
ambient density	kg/m^3	998.2
excess fractional density	kg/m^3	2.0
inlet velocity	m/s	0.079
k_0	$m^2.s^{-2}$	6.875×10^{-5}
ε_0	$m^2.s^{-3}$	1.38×10^{-5}

For simulation, 30 layers with grids of dimension of 0.05m in x-direction have been used to construct the domain. The simulation time was 300s and a time step of 0.05s has been used. Figure 2 presents the measured and simulated velocity profiles at x=0.9m and x=2.4m. These profiles have been normalized using their own outer flow scales u_{max} and $y_{0.5}$. The outer length scale $y_{0.5}$ is defined as the height at which the velocity u is equal to half the maximum velocity u_{max}. Acceptable agreement has been obtained for both models; away from the boundary, EARSM shows closer values to measured data.
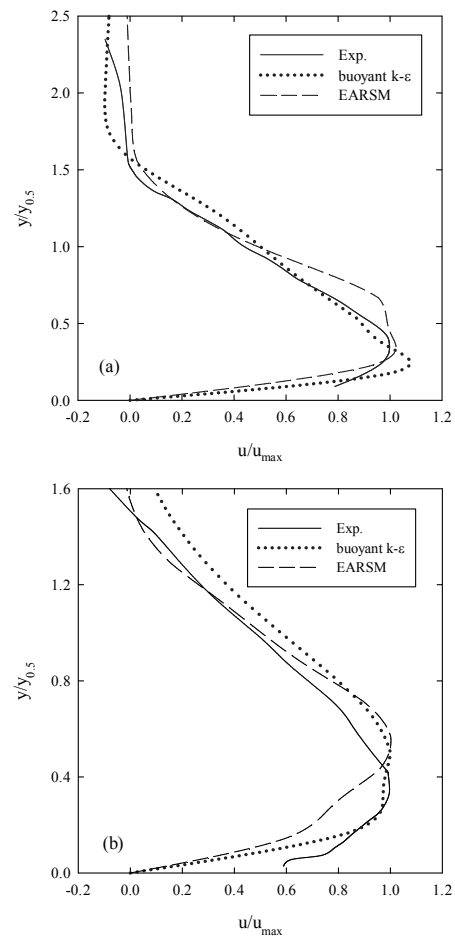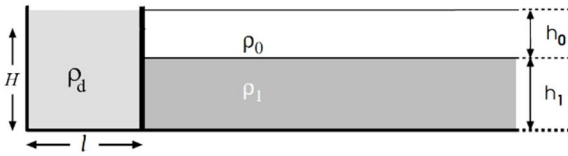

Figure 2. Velocity profiles of turbulence models and measured values at (a) x=0.9m and (b) x=2.4m in experiment of Gerber [34]

**Table 3. Summary of simulation setup in experiments of Sutherland et al. [35]**

Case #	H (cm)	h_o (cm)	h_1 (cm)	ρ_o (kg/m³)	ρ_1 (kg/m³)
1	20	10	10	1000	1020
2	20	17.5	2.5	1000	1020

**Figure 3. Sketch of lock-exchange experiment of Sutherland et al. [35]**

The third series of simulation cases are performed to identify the propagation dynamics of intrusive gravity currents. The simulations are compared with the experimental measurements of Sutherland et al. [35]. The experiments have been conducted in a flume with 197.1cm length, 17.6cm width and 48.5cm height. The lock-length (*l*) behind the gate is fixed at 18.6cm and the total water depth (*H*) is set equal to 20cm (Figure 3). Two tests have been selected for simulation. In both simulation cases, the density of the lock fluid (ρ_d) is equal to the depth-weighted average of the upper and lower layers. In the first case, the depth of the two layers in the ambient fluids is also equal ($h_o=h_1$). In the second case however, the depth of the two layers in the ambient fluids is not equal. Table 3 shows the initial conditions for the simulations. The computational grid size in the *x* and *z* directions are set to 5.0*mm*.

In the first symmetrical case, the simulation snapshots are created to visualize the temporal evolutions of the intrusive gravity current. Figure 4 shows that the fluid contained behind the lock gate collapses symmetrically and propagates along the interface after the removal of lock gate, and the head is visible after 2s. The initial collapse begins with rapid acceleration and the current head becomes uniform in shape after 26*s*. As it propagates to the right end of the wall, the head of the gravity current causes strong mixing, resulting in mass loss and dilution in the head. The temporal evolution of the gravity current is illustrated with images taken from the experiments and the graphics obtained from numerical simulations as shown in Figure 4. It shows that the numerical model prediction with either buoyant *k-ε* or EARSM turbulence closures describe the dynamics of intrusive gravity current with a symmetrical condition. It is also evident that the numerical model resolves the fine scales associated with the mixing that occur in the vicinity of the gravity current head. The formation of Kelvin-Helmholtz billows that show the vertical structure behind the head of intrusive gravity current, is reproduced well by both closure schemes. However, overall shape of the current is closer to experimental results in case of EARSM, especially in the head region. The traveling distance calculated from both buoyant *k-ε* and EARSM closures are plotted as a function of time in Figure 5, which show very good agreements with experimental measurements. In the second case (Figure 6), a different dynamics compared to the symmetrical case (case 1) has been
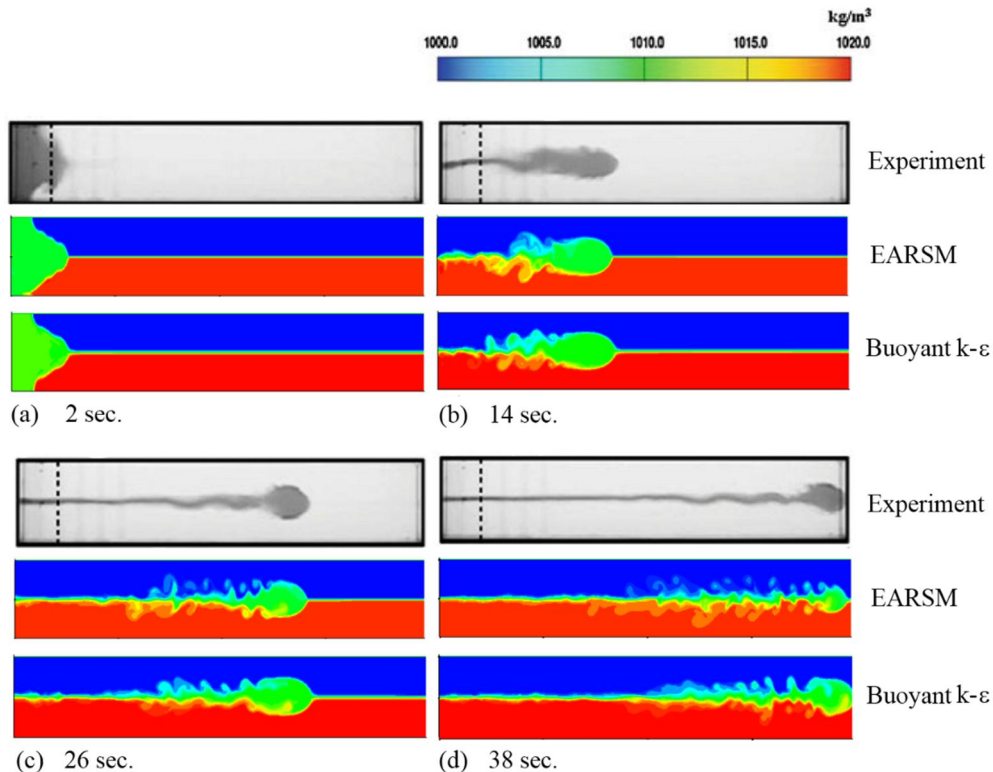
Figure 4. Temporal evolutions of an intrusive gravity current for case 1, where experimental results of Sutherland et al. [35] are compared with simulated density contours based on buoyant k-ε and EARSM turbulence closures.
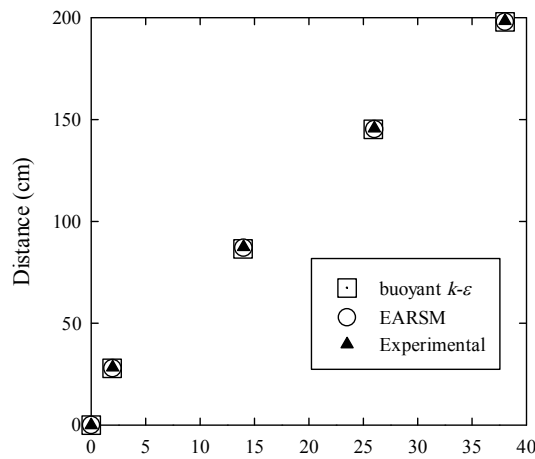
**Figure 5. Traveling distance of intrusive gravity current as a function of time in case 1, for simulated values of buoyant k-ε and EARSM closures and measured values [35]**

structured. In this case, the propagation speed is observed to be slower than that of the case 1, in particular, the gravity current does not form a symmetrical head as it propagates. This is because the return flows in the upper layer and lower layer of the ambient fluid move at different speeds and they interact with the end wall differently. Sutherland et al. [35] also mentioned that due to the small density difference between lock and ambient upper-layer fluid, the top return flow takes longer to be established, resulting in mixing between the lock and ambient fluid behind lock-gate, whereas the return flow in the lower layer of the ambient fluid intrudes

into the lock fluid rapidly with weak vorticity. After the collapse phase, the lock fluid forms the head and tail of the gravity current. Shear instability occurs only across the interface between the gravity current and the upper layer. The shape of the gravity current seems similar to a gravity current propagating over a no-slip bottom.

By comparing the experimental and simulation results at t=14s, the predictions show less mixing, whilst some initial mixing is introduced by vorticity in the upper lighter layer behind lock gate. After the collapse phase, the numerical simulations also show weaker shear instabilities in the rear part of the tail region (Fig. 6c). Sutherland et al. [35] note that the mixing between lock fluid and the upper-later ambient fluid is promoted by the vorticity created by the gate removal. In both cases of buoyant k-ε and EARSM models, the vorticity developed by the lock-gate removal cannot be simulated. However, the propagation speed of the intrusive current is still correctly reproduced by the numerical simulations.

The last test is based on the experimental study accomplished by Zhu et al. [36] as a lock-exchange type of gravitational flow. The experiments were carried out in a rectangular Perspex flume, 200mm wide, 400mm deep and 2590mm long. The flume was filled with fresh water to a depth of H_0=100mm and a Perspex gate was positioned vertically at a distance x_0=200mm away from the left end of the channel to form a lock. Salt was dissolved into the water behind
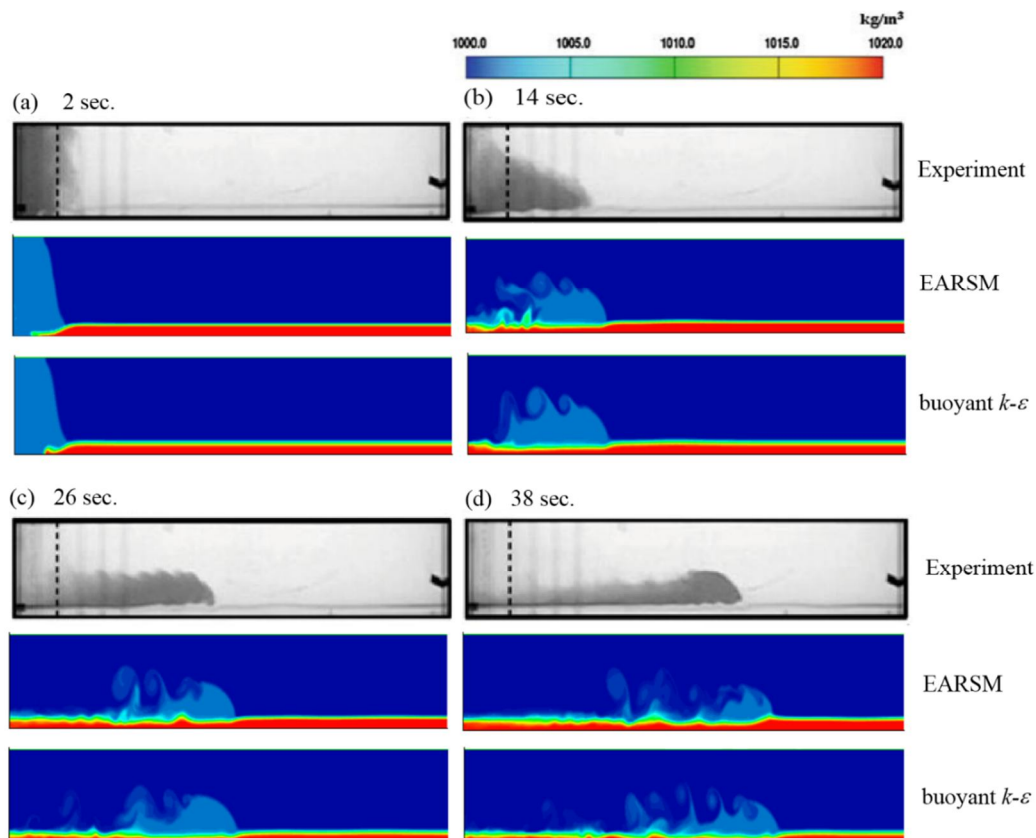
Figure 6. Temporal evolutions of an intrusive gravity current for case 2, where experimental results of Sutherland et al. [35] are compared with simulated density contours based on buoyant k-ε and EARSM turbulence closures.

50

the Perspex gate to create a density difference between the two parts of the flume. A densimeter was used to measure the densities of saline and fresh waters. Densities of ρ_a=1009.5 and ρ_0=999.5 kg/m^3 were used for saline and fresh waters, respectively, corresponding to a density difference of $\Delta\rho = \rho_a - \rho_0 = 10$ kg/m^3. Zero velocity boundary conditions were implemented at solid walls. In order to accurately simulate the hydrodynamic parameters of the gravity current flow and the salinity concentration within the water, a grid dependency study should be carried out. For a coarse gridding, the solution will be sensitive to the grid resolution. With the grid refinement, the computational cost increases but the solution becomes insensitive to the grid resolution. The aim is, therefore to find the coarsest possible grid, requiring the lowest computational effort, while remaining insensitive to the grid resolution. A grid

independent solution was found by simulating the same gravity current on successively refined grids. The reference mesh was 10×150 (10 layers and 150 cells in x-direction). Different number of layers and grids in x-direction were utilized for both turbulence closures, respectively. The time step in each case was adjusted according to the cell size characteristics, and the simulation time was 62s. Figure 7 shows that, for both turbulence models, grid independent profiles are obtained for grids 12×150 and finer (time and front position values are in non-dimensional form $x_f^* = \frac{x_f}{x_0}$, $t^* = \frac{t}{t_0}$, $t_c = \frac{x_0}{(g'H_0)^{1/2}}$, $g' = \frac{g\Delta\rho}{\rho_a}$).

Figure 8 shows the gravity current profiles for buoyancy-modified k-ε and EARSM turbulence closures. The front position at successive times after
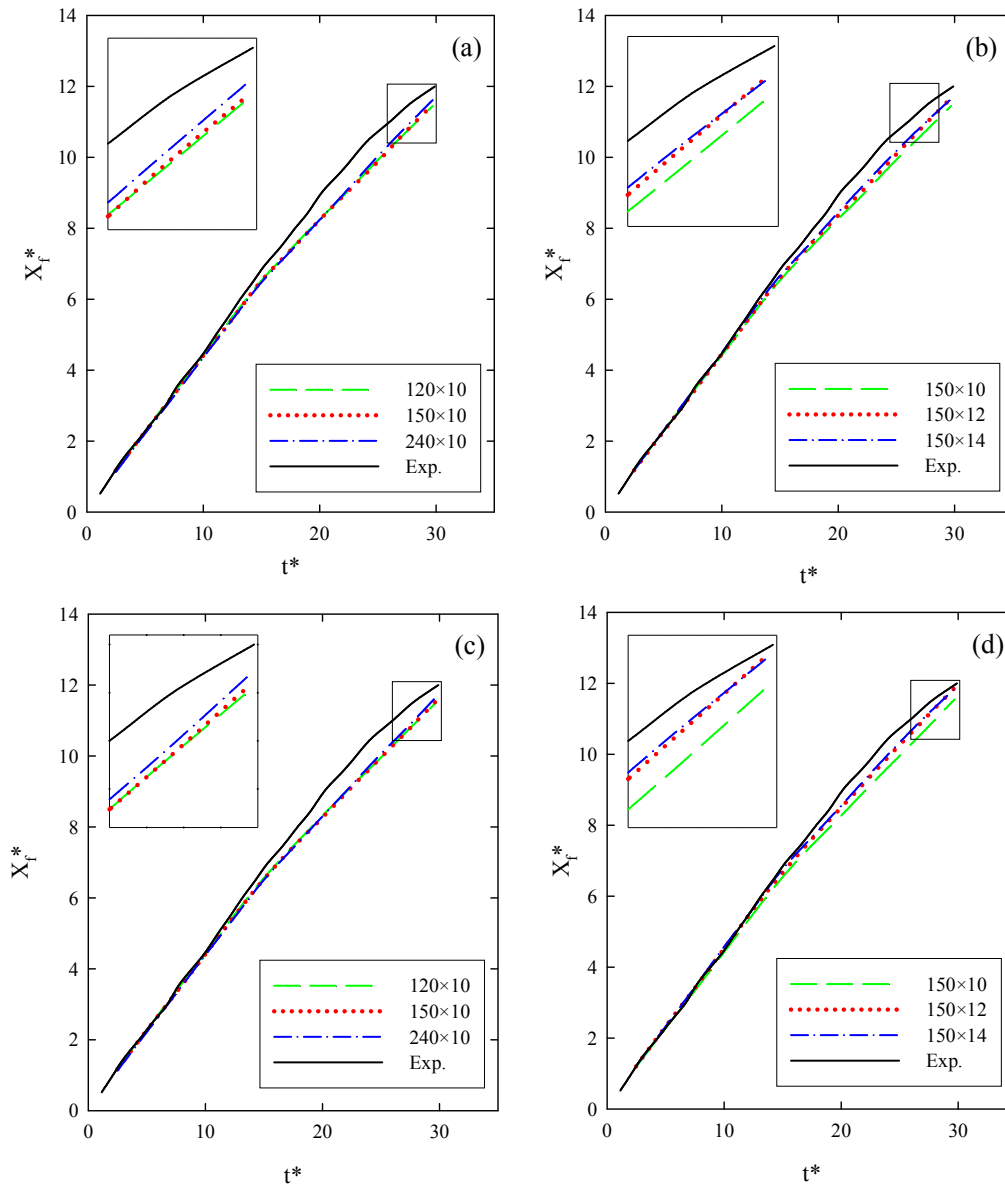

Figure 7. Simulated front position profiles for different grid resolutions with buoyant k-ε (a and b) and EARSM (c and d) turbulence closures in experiment of Zhu et al. [36]
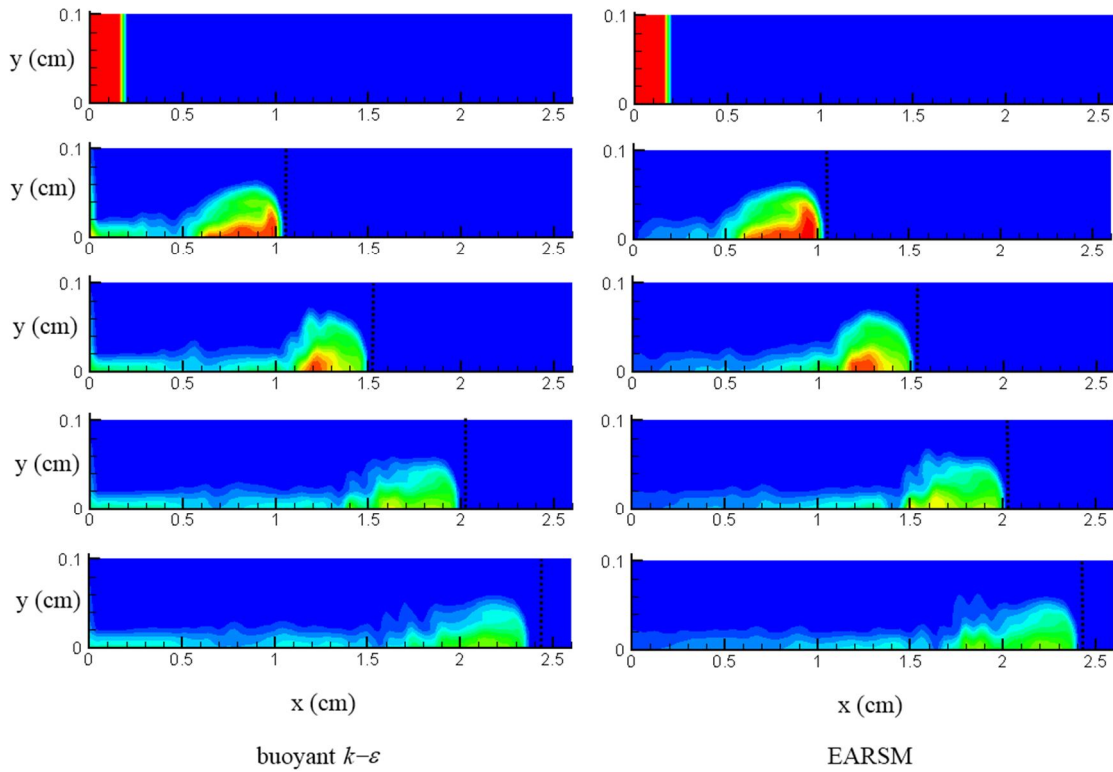
51

Figure 8. Results of simulated salinity distribution for EARSM and buoyant k-ε turbulence closures at 0, 23, 36, 52 and 62s in experiments of Zhu et al. [36]. The dotted line in the frames is the experimentally reported location of the nose of the gravity

the release has been reported [36]. Also, Figure 9 shows the front position of the gravitational current versus time for simulated results and measured values of Zhu et al. in non-dimensional form. During an initial slumping phase, the front head position x_f, increases linearly with time. Two distinct phases of lock-exchange front propagation were observed and at
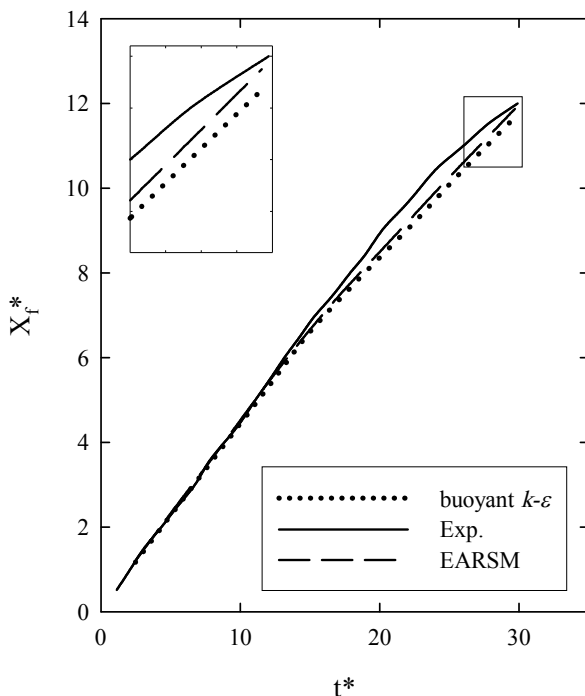

Figure 9. Comparison of front head position for EARSM and buoyant k-ε turbulence closures with measured values of Zhu et al. [36]

about 10 lock lengths, the transition from the first to the second phase occurs [36]. While in the first phase of the gravitational flow extent, both models predict the front head position well, the k-ε model shows a little more underestimation in the second phase. Figure 10 shows the velocity profiles of EARSM and k-ε turbulence models in comparison with measured values at x=1020, 1040, 1060 and 1080mm respectively, and at t=12.28s. It is evident that EARSM turbulence closure predicts the velocities more accurately, with the exception of near bed values. This may justify the need for further research for improvement of appropriate wall functions for Reynolds stresses.

4. Conclusion

Lock-exchange, wall jet and intrusive gravity currents were simulated to investigate the effects of using two different turbulence closures, a two equation standard k-ε model with buoyancy terms and an Explicit Algebraic Reynolds Stress Model (EARSM) along with an Explicit Algebraic Scalar Flux Model (EASFM). Results show that, the EARSM provides better predictions for velocity profiles especially in the far zone from the bed. Also, EARSM provides better predictions for the front head position. However, using appropriate wall functions for Reynolds stresses could augment accuracy of model in boundary layers. Because the EARSM turbulence model provides better predictions in most parts of the stratified gravity currents, while its computational
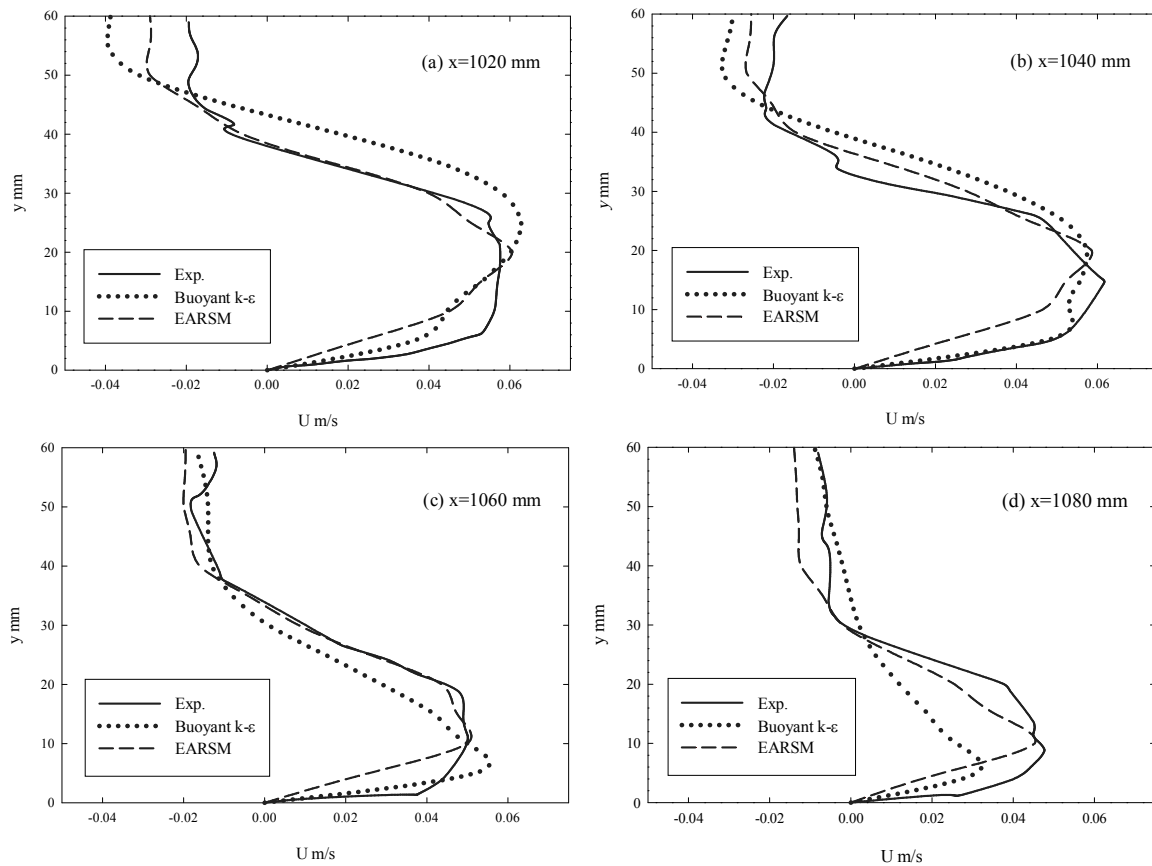
Figure 10. Velocity profiles of turbulence models and measured values at (a) *x*=1020mm, (b) *x*=1040mm, (c) *x*=1060mm and (d) *x*=1080mm in experiments of Zhu et al. [36]

costs is not considerably greater than two-equation models, it can be concluded that in these category of flows, using EARSM model is reasonable and may be suggested. It is also worth noting that a distinct turbulence model cannot satisfactorily predict all turbulent flow cases, and especial calibration for constants and consideration for source terms are needed**.**

5. References

1- Simpson, J., (1997), *Gravity currents in the environment and the laboratory*, Cambridge University Press.

2- Huppert, H.E. and Simpson, J.E., (1980), *The slumping of gravity currents*, Journal of Fluid Mechanics., 99: 785-799.

3- Garcia, M.H., (1993), *Hydraulic jumps in sediment-driven bottom currents*, Journal of Hydraulic Engineering, 119: 1094-1117.

4- Islam, M. A., and Imran, J., (2010), *Vertical structure of continuous release saline and turbidity currents*, Journal of Geophysical Research: Oceans (1978–2012), 115(C8).

5- Xu, D., and Chen, J., (2012), *Experimental study of stratified jet by simultaneous measurements of velocity and density fields*, Experiments in fluids, 53(1), 145-162.

6- Ivey, G. N., Winters, K. B. and Koseff, J.R., (2008), *Density stratification, turbulence, but how much mixing?*, Annual Review of Fluid Mechanics, 40(1), 169.

7- Hartel, C., Meiburg, E. and Necker, F., (2000), *Analysis and direct numerical simulation of the flow at a gravity-current head. Part 1. Flow topology and front speed for slip and no-slip boundaries*, Journal of Fluid Mechanics, 418: 189-212.

8- Necker, F., Hartel, C., Kleiser, L. and Meiburg, E., (2002), *High-resolution simulations of particle-driven gravity currents*, International Journal of Multiphase Flow, 28: 279-300.

9- Cantero, M.I., Balachandar, S., García, M.H. and Bock, D., (2008), *Turbulent structures in planar gravity currents and their influence on the flow dynamics*, Journal of Geophysical Research, 113(C8), C08018.

10- Ooi, S. K., Constantinescu, G. and Weber, L.J., (2007), *2D large-eddy simulation of lock-exchange gravity current flows at high Grashof numbers*, Journal of Hydraulic Engineering, 133(9), 1037-1047.

11- Scotti, A., (2008), *A numerical study of the frontal region of gravity currents propagating on a free-slip boundary*, Theoretical and Computational Fluid Dynamics, 22(5), 383-402.

12- Choi, S. and Garcia, M.H., (2002), *k-ε turbulence modeling of density currents developing two dimensionally on a slope*, Journal of Hydraulic Engineering, 128: 55-63.

13- Imran, J., Kassem, A. and Khan, S.M., (2004), *Three-dimensional modeling of density current. I.*

Flow in straight confined and unconfined channels, Journal of Hydraulic Research, 42: 578-590.

14- Huang, H., Imran, J. and Pirmez, C., (2005), *Numerical model of turbidity currents with a deforming bottom boundary*, Journal of Hydraulic Engineering, 131: 283-293.

15- Elliott, Z.A. and Venayagamoorthy, S.K., (2011), *Evaluation of turbulent Prandtl (Schmidt) number parameterizations for stably stratified environmental flows*, Dynamics of Atmospheres and Oceans, 51(3), 137-150.

16- Hellsten, A. and Wallin, S., (2009), *Explicit algebraic Reynolds stress and non-linear eddy-viscosity models*, International Journal of Computational Fluid Dynamics, 23(4), 349-361.

17- Rodi, W., (1976), *A new algebraic relation for calculating the Reynolds stresses*, In Gesellschaft Angewandte Mathematik und Mechanik Workshop Paris France, Vol. 56, p. 219.

18- Gatski, T.B. and Speziale, C.G., (1993), *On explicit algebraic stress models for complex turbulent flows*, Journal of Fluid Mechanics, 254, 59-78.

19- Girimaji, S.S., (1996), *Fully explicit and self-consistent algebraic Reynolds stress model*, Theoretical and Computational Fluid Dynamics, 8(6), 387-402.

20- Jongen, T. and Gatski, T.B., (1999), *A unified analysis of planar homogeneous turbulence using single-point closure equations*, Journal of Fluid Mechanics, 399(1), 117-150.

21- Wallin S., Johansson A.V., (2000), *An explicit algebraic Reynolds stress model for incompressible and compressible turbulent flows*, Journal of Fluid Mechanics, 403: 89-132.

22- Hejazi, K., (2004), *3D numerical modelling of flow and turbulence in oceanic water bodies using an ALE projection method*, The First Seminar On Computer Simulation In Civil Engineering, K.N.T. University of Technology, Iran.

23- Rodi, W., (1984), *Turbulence models and their applications in hydraulics, a State of the arts Review*, University of Karlsruhe, Germany.

24- Rodi, W., (1987), *Examples of calculation methods for flow and mixing in stratified fluids*, Geophysical Research Journal, vol.92, No.C5, pp. 5305-5328.

25- Gibson, M.M. and Younis, B.A., (1986), *Calculation of swirling jets with a Reynolds stress closure*, Physics of Fluids, 29(1): 38-48.

26- Walker, D.T. and Chen, C.Y., (1996), *Evaluation of algebraic stress modeling in free-surface jet flows*, Journal of Fluids Engineering, 118(1): 48-54.

27- Pope, S.B., (1975), *A more general effective-viscosity hypothesis*, Journal of Fluid Mechanics, 72(2): 331-340.

28- Rodi, W., (1979), *Turbulence models for environmental problems*, In Von Karman Inst. for Fluid Dynamics: Prediction Methods for Turbulent Flows (Vol. 1).

29- Hua, Z., Gu, L., Xing, L. and Dai, W., (2009), *New explicit algebraic stress and flux model for active scalar and simulation of shear stratified cylinder wake flow*, Science in China Series E: Technological Sciences, 52, 2536–2546.

30- Wikström, P.M., Wallin, S. and Johansson, A.V., (2000), *Derivation and investigation of a new explicit algebraic model for the passive scalar flux*, Physics of Fluids, 12(3): 688-702.

31- Chorin, A.J., (1968), *Numerical solution of the Navier-Stokes equations*, Mathematics of Computation Journal, vol.22, pp. 745-762.

32- Temam, R., (1969), *Sur l'approximation de la solution des equation de Navier-Stokes par la méthode des pas fractionnaires*, Archive for Rational Mechanics and Analysis, vol.32, pp. 135-153.

33- Kneller, B., Bonne, S. and McCaffrey, W., (1999), *Velocity structure, turbulence and fluid stresses in experimental gravity currents*, Journal of Geophysics Research, VOL. 104, NO .C3, 5381-5391.

34- Gerber, G., (2008), *Experimental measurement and numerical modelling of velocity, density and turbulence profiles of a gravity current*, PhD thesis, University of Stellenbosch.

35- Sutherland, B.R., Kyba, P.J. and Flynn, M.R., (2004), *Intrusive gravity currents in two-layer fluids*, Journal of Fluid Mechanics, 514, 327-353.

36- Zhu, J.B., Lee, C.B., Chen, G.Q. and Lee, J.H.W., (2006), *PIV observation of instantaneous velocity structure of lock release gravity currents in the slumping phase*, Communications in Nonlinear Science and Numerical Simulations, 11, 262–270.